J Mater Sci (2010) 45:1553–1559
DOI 10.1007/s10853-009-4123-2

Luminescence properties of double-perovskite $Sr_2Ca_{1-2x}Eu_xNa_xMoO_6$ red-emitting phosphors prepared by the citric acid-assisted sol–gel method

Zhiguo Xia · Jianfeng Sun · Haiyan Du · Daimei Chen · Jiayue Sun

Received: 16 June 2009 / Accepted: 9 December 2009 / Published online: 29 December 2009

Abstract Double-perovskite $Sr_2Ca_{1-2x}Eu_xNa_xMoO_6$ red-emitting phosphors were prepared by the citric acid-assisted sol–gel method, and their luminescence properties were investigated as a function of sintering temperature and Eu^{3+}-doping concentration. B-site substituted $Sr_2Ca_{0.8}Eu_{0.1}Na_{0.1}MoO_6$ phosphor, in which Na^+ ions act as charge compensators, was selected to study the thermal behavior, phase structure, microstructure, and photoluminescence property under different sintering temperatures. The photoluminescence studies on $Sr_2Ca_{1-2x}Eu_xNa_xMoO_6$ ($x = 0.02$, 0.05, 0.10, 0.15, 0.2) show that a dominant red emission line at around 594 nm, which is due to the Eu^{3+} magnetic dipole transition of $^5D_0$–$^7F_1$, is observed under different Eu^{3+} excitations (396 and 412 nm). Further, Eu^{3+} dopant content dependent emission spectra investigations of $Sr_2Ca_{1-2x}Eu_xNa_xMoO_6$ phosphors indicates that, when the Eu^{3+} concentrations $x = 0.05$, there are minimum differences between the emission intensity of $^5D_0$–$^7F_1$ transition at 594 nm and that of $^5D_0$–$^7F_2$ transition at 615 nm. With increasing Eu^{3+} concentration, the variation of the emission intensities between the two transitions keep nearly invariable and $Sr_2Ca_{0.8}Eu_{0.1}Na_{0.1}MoO_6$ phosphor has the strongest red emission in this series.

Z. Xia (✉) · D. Chen
School of Materials Sciences and Technology, China University of Geosciences, Beijing 100083, China
e-mail: xiazg426@yahoo.com.cn

J. Sun · H. Du · J. Sun (✉)
College of Chemistry and Environmental Engineering, Beijing Technology and Business University, Beijing 100048, China
e-mail: jiayue_sun@126.com

Introduction

White light-emitting diodes (w-LEDs) are considered as the next-generation light source because of their high luminous efficiency, long lifetimes, low environmental impact, and small structure type [1, 2]. Among them, phosphor-converted w-LEDs have the enough interests in the industrial and academic fields, and there are two ways to realize the white light emission [3]. One scheme is the combination of the blue LEDs chip and the yellow-emitting phosphor, and the other is the combination of the near ultraviolet (NUV) LEDs chip and the red-, green- and blue-emitting phosphors [4]. For the first scheme, it is based on blue LED plus yellow phosphor, which has low color-rendering index (CRI) because of lack of red component in their spectra [5]. As expected, red-emitting phosphor used to compensate yellow-emitting phosphor is introduced to improve the CRI and increase the light conversion efficiency [6]. Similarly, for the second scheme, NUV light-excitable red-emitting phosphor for w-LEDs is also essential [7]. Hence, there has been a widespread and growing interest in developing new families of red-emitting phosphors with high absorption in the near UV to blue region [8–10].

Tungstate and molybdate are two families as the hosts of phosphors that have promising applications as the red component of w-LEDs, and the incorporation of Eu^{3+} into tungstate and molybdate crystal lattice modifies the luminescence spectra due to the formation of the emission centers that generate the specific red light [11–14]. Recently, there are many reported references on novel tungstate and molybdate red-emitting phosphors, such as $LiEuM_2O_8$ (M = Mo, W) [11], $R_{2-x}Eu_x(MoO_4)_3$ (R = La, Y, Gd) [12], $(Ca, Eu, M)(WO_4)_{1-z}(MoO_4)_z$ (M = Mg, Zn) [13], $M_5Eu(WO_4)_{4-x}(MoO_4)_x$ (M = Li, Na, K) [14], and

so on. Among them, a kind of double-perovskites A_2CaMO_6 (A = Sr, Ba; M = Mo, W) used as red component of w-LEDs has attracted many scientists' attentions [15–17]. This is ascribed to that the physical properties of double-perovskites $AB_{1/2}B'_{1/2}O_3$ are strongly influenced by the degree of B-cation ordering, and then color-tunable luminescence properties can be detected. Thus, we selected Sr_2CaMoO_6 as a potential red-emitting phosphor in this study.

Among the previously reported references, many tungstate and molybdate phosphors were synthesized by conventional solid-state reaction method [11–17]. Therefore, the aggregation and inhomogeneous shape are unavoidable, which inhibit the absorption of the excitation energy and, therefore, reduce the emission intensity. Sol–gel method is one of the most important "soft chemistry" techniques for the synthesis of phosphor materials with higher uniformity in particle size distribution, non-agglomeration and higher photoluminescence intensity [18]. In this article, to the best of our knowledge, we first reported the preparation of double-perovskites Sr_2CaMoO_6 red-emitting phosphors by sol–gel process and their luminescence properties.

Experimental

Red-emitting phosphors, $Sr_2Ca_{1-2x}Eu_xNa_xMoO_6$ ($x = 0.02$, 0.05, 0.10, 0.15, 0.2), were prepared by the citric acid-assisted sol–gel method. The starting materials used in the preparation were $Sr(NO_3)_2{\cdot}6H_2O$ (analytical reagent, A.R.), $Ca(NO_3)_2{\cdot}6H_2O$ (A.R.), $(NH_4)_6Mo_7O_{24}{\cdot}4H_2O$ (A.R.), Eu_2O_3 (99.999%), Na_2CO_3 (A.R.), HNO_3 (A.R.), citric acid (A.R.), and deionized water. According to the chemical formulas stated above, stoichiometric amount of Eu_2O_3 was dissolved in dilute HNO_3 (A.R.) under vigorous stirring. Then stoichiometric amount of $Sr(NO_3)_2{\cdot}6H_2O$, $Ca(NO_3)_2{\cdot}6H_2O$, $(NH_4)_6Mo_7O_{24}{\cdot}4H_2O$, and a suitable volume of deionized water was added and stirred homogenously. Citric acid was added to the solution as chelating agent for the metal ions. The molar ratio of total chelate metal cations to citric acid was 1:1.5. At the end, the pH value of the final solution was adjusted to 7, 8 by the addition of suitable amount of dilute $NH_3{\cdot}H_2O$. Finally, the highly transparent solution was obtained after stirring for a few minutes. Then the transparent solution was heated at 353 K in oven to get transparent light-brown sol, and the sol was further dried at 403 K in oven for 48 h to get dried gel. The dried gel was annealed at 873 K for 12 h in air to get the foamed precursor, and the precursor was further sintered at different temperatures for 8 h in air to get the white phosphor powder.

Thermogravimetry–differential thermal analyzer (TG-DTA) for the dried gel and sintered precursor at 873 K were performed on a SHIMADZU model DTG-60AH TG-DTA instrument. The analyzer was operated at a heat rate of 2 K/min from room temperature to a maximum temperature of 1373 K. The X-ray diffraction (XRD) patterns were recorded by using a SHIMADZU model XRD-6000 X-ray powder diffractometer (Cu Kα radiation, 40 kV, 30 mA, and a scanning speed 2.0° $(2\theta)\text{min}^{-1}$). Fourier transform infrared spectroscopy (FT-IR) data were collected on a FTIT-AVATAR370 spectrophotometer over the range of wavenumber 4000–400 cm^{-1}, and the standard KBr pellet technique was employed. A scanning electron microscope (SEM, JEOL, JSM-6490) was employed to analyze the size and shape of the selected samples. Diffuse reflection spectra of as-synthesized phosphor powder samples were measured on a UV-Vis-NIR spectrophotometer (UV-3600, SHIMADZU) attached to an integral sphere. $BaSO_4$ was used as a reference standard. The excitation and emission spectra were recorded by using a Perkin–Elmer LS-55 fluorescence spectrophotometer with a photomultiplier tube operating at 400 V, and a 150 W Xe lamp was used as the excitation lamp. All the measurements for the as-synthesized samples were performed at room temperature.

Results and discussion

TG-DTA analysis

Figure 1 gives the TG-DTA curves of dried gel (a) and sintered precursors at 873 K (b) of $Sr_2Ca_{0.8}Eu_{0.1}Na_{0.1}MoO_6$. In order to understand the pyrolysis behavior of the complex dried gel, Fig. 1a indicates that the weight loss of the dried gel occurs in the TG curve from room temperature to 789 K, which also corresponds to a strong endothermic peak at about 682 K in DTA curve. This stage should originate from the decomposition and burning of organic chelate agents. After that, a small exothermic peak at about 944 K is shown in the DTA curve, and it also shows an obvious weight loss in TG curve, which is attributed to the decomposition of metal nitrics in the starting materials. Finally, there is a weak endothermic peak at about 1131 K in DTA curve, but no obvious weight loss can be found in TG curve. Therefore, it indicates that the $Sr_2Ca_{0.8}Eu_{0.1}Na_{0.1}MoO_6$ phase is formed completely. Further, in Fig. 1b, TG-DTA curves of $Sr_2Ca_{0.8}Eu_{0.1}Na_{0.1}MoO_6$ precursor sintered at 873 K were also investigated, and we also found the similar weight loss and thermal behavior for the formation of the $Sr_2Ca_{0.8}Eu_{0.1}Na_{0.1}MoO_6$ phase above 873 K. Therefore, we conclude that crystalline $Sr_2Ca_{0.8}Eu_{0.1}Na_{0.1}MoO_6$ phase can start to be partly formed after the decomposition of metal nitrics after 944 K, and then will be formed above 1073 K.

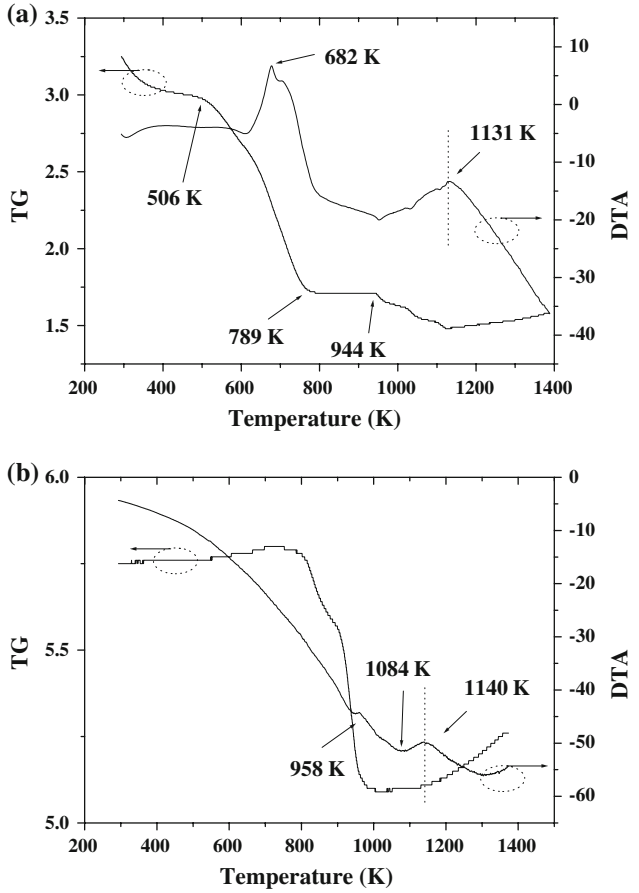

Fig. 1 TG-DTA curves of $Sr_2Ca_{0.8}Eu_{0.1}Na_{0.1}MoO_6$ dried gel (**a**) and sintered precursors at 873 K (**b**)

XRD analysis

Two cation sites (Sr at the A-site and Ca at the B-site) in double-perovskite Sr_2CaMoO_6 phase can be substituted by Eu^{3+}, and previous research also indicates that B-site substitution sample helps in the formation of pure double-perovskite Sr_2CaMoO_6 phase [15]. Further, it is found that the introduction of the charge compensators can obviously improve the emission intensity of Eu^{3+}-doped Sr_2CaMoO_6. Therefore, B-site-substituted $Sr_2Ca_{0.8}Eu_{0.1}Na_{0.1}MoO_6$ sample was selected in this study, in which Na^+ acts as the charge compensator. Figure 2 exhibits the XRD patterns of the precursor and the $Sr_2Ca_{0.8}Eu_{0.1}Na_{0.1}MoO_6$ samples obtained by sintering the precursor at different temperatures. As shown in Fig. 2, the XRD pattern of the precursor sintered at 873 K shows complex crystallization phases, including the $SrMoO_4$, $CaMoO_4$, and Sr_2CaMoO_6 phases. When the sintering temperature reaches 1073 K, most diffraction peaks in XRD pattern can be indexed to Sr_2CaMoO_6 phase except for the impurity peaks at 27.7°, which is corresponding to the $SrMoO_4$ phase [15]. With increasing sintering temperature, the intensity of the

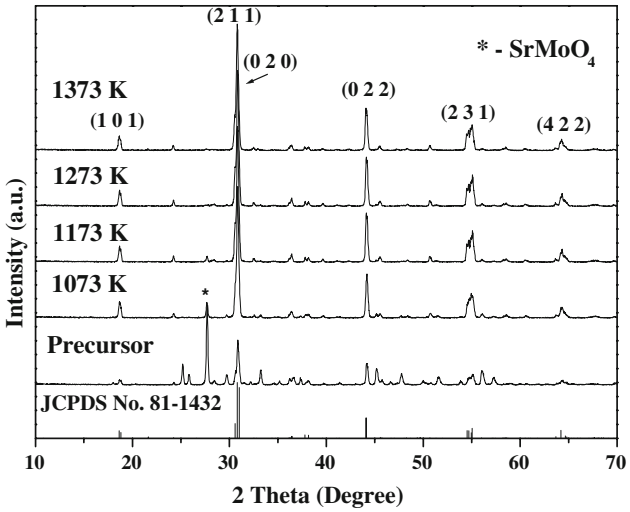

Fig. 2 XRD patterns of the precursor and the $Sr_2Ca_{0.8}Eu_{0.1}Na_{0.1}MoO_6$ samples obtained by sintering the precursor at different temperatures

impurity peak at 27.7° gradually decreases, and the impurity peak completely disappears when the sintering temperature reaches 1173 K, which is consistent with the TG-DTA analysis. Simultaneously, the peak positions agree well with those of the standard pattern (JCPDS NO. 81-1432) for double-perovskite structure Sr_2CaMoO_6, which belongs to the monoclinic crystal system with a space group of $P2_1/n$. Further, according to some previous reports [19, 20], the lattice constants of double-perovskite Sr_2CaMoO_6 are: $a = 5.762$ Å, $b = 5.848$ Å, $c = 8.187$ Å, and $\beta = 90.194°$.

The above results also show that the crystallization temperature of pure double-perovskite Sr_2CaMoO_6 phase through the present citric acid-assisted sol–gel method is lower than that in the conventional solid-state reaction (1473 K for 24 h), which demonstrates the most essential advantage of the sol–gel method [15–17].

FT-IR analysis

The FT-IR spectra of the as-synthesized precursor sintered at 873 K, and the $Sr_2Ca_{0.8}Eu_{0.1}Na_{0.1}MoO_6$ samples obtained by sintering the precursor at different temperature are shown in Fig. 3. As shown in Fig. 3, the bands at 3430 and 1632 cm^{-1} are assigned to O–H stretching vibration and H–O–H bending vibration of absorbed water molecular from air, respectively, and it is completely different from coordinated water in compounds [21]. For the FT-IR spectrum of the as-synthesized precursor, the 1474 cm^{-1} band is attributed to N–O vibration modes from the starting reactants NO^{3-}, while no obvious absorption band can be found in this region for the $Sr_2Ca_{0.8}Eu_{0.1}Na_{0.1}MoO_6$ samples obtained by sintering the precursor at different

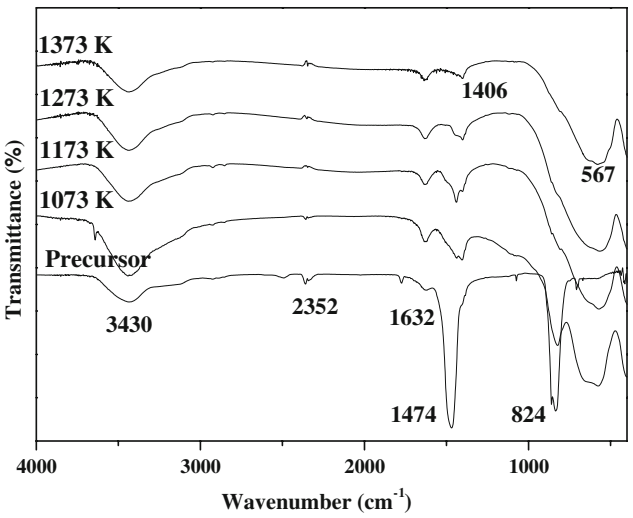

Fig. 3 FT-IR spectra of the precursor and the $Sr_2Ca_{0.8}Eu_{0.1}Na_{0.1}MoO_6$ samples obtained by sintering the precursor at different temperatures

temperatures. This is also consistent with the previous TG-DTA analysis. The absorption band around 824 cm^{-1} is related to O–Mo–O stretches of the MoO_4^{2-} groups, because of the existence of the $SrMoO_4$ impurity phase [15, 22]. And this absorption band disappears for the sample obtained above 1173 K. Furthermore, a strong absorption band around 567 cm^{-1} is formed when the sintering temperature is above 1073 K, and the four samples have nearly the same vibration bands in this wavenumber region, which is related to MoO_6^{6-} groups in Sr_2CaMoO_6 structure [17, 22, 23]. The above results indicate that the products obtained at 1073 and 1373 K are of the same phase Sr_2CaMoO_6 with different crystallization.

SEM micrographs analysis

In order to further understand the growth process of the $Sr_2Ca_{0.8}Eu_{0.1}Na_{0.1}MoO_6$ samples, we investigated the effects of temperature on the morphology of the products. Figure 4 shows the SEM images of the $Sr_2Ca_{0.8}Eu_{0.1}Na_{0.1}MoO_6$ samples, which is obtained by sintering the precursor at different temperatures (1073, 1173, 1273, and 1373 K) for 8 h. It can be seen from Fig. 4 that there is an obvious grain growth trend with increasing temperature. Figure 4a, as an example, these are the smallest grain size (1–2 μm). Further, the phosphor powder grains sintered at 1173 K grow up to 2–3 μm, and the phosphor powder has the moderate grain size (3–5 μm), uniform shaped microstructure at 1273 K. Then the larger grain (∼5 μm) can be found when the reaction temperature reaches 1373 K. Compared to the solid-state method, the small particle size and uniform surface morphology of the $Sr_2Ca_{0.8}Eu_{0.1}Na_{0.1}MoO_6$ samples by sol–gel method can better meet the application of phosphors in LED.

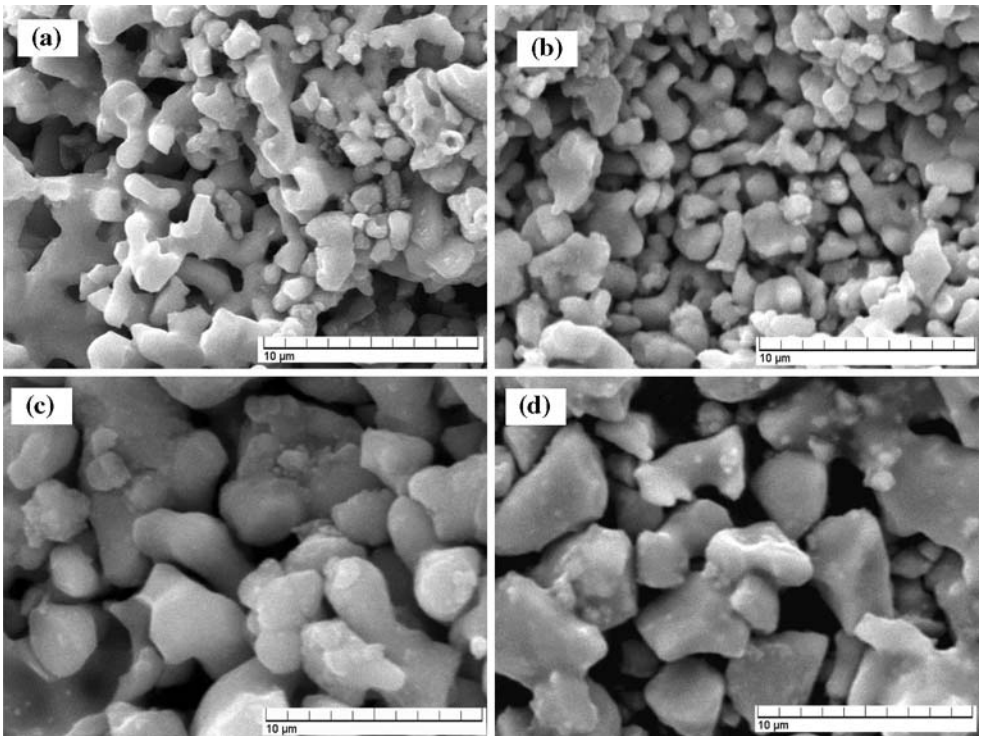

Fig. 4 SEM images of the $Sr_2Ca_{0.8}Eu_{0.1}Na_{0.1}MoO_6$ samples obtained by sintering the precursor at different temperatures, **a** 1073 K, **b** 1173 K, **c** 1273 K, and **d** 1373 K

Photoluminescence analysis

In order to investigate the energy absorption of the different samples, Fig. 5 gives the diffuse reflection spectra of the precursor and the $Sr_2Ca_{0.8}Eu_{0.1}Na_{0.1}MoO_6$ samples obtained by sintering the precursor at different temperature. As shown in Fig. 5, broad absorption band is observed for all compositions, and this band is due to charge transfer (CT) transition from oxygen to molybdenum (O–Mo) [24]. However, the largest absorption band for the precursor is centered at 255 nm, which should be ascribed to the MoO_4^{2-} groups in the $SrMoO_4$ phase [15]. However, when the precursor is secondly sintered above 1073 K, it is observed that the $Sr_2Ca_{0.8}Eu_{0.1}Na_{0.1}MoO_6$ shows a platform of high reflection in the wavelength range of 450–700 nm and then starts to decrease obviously from 450 to 200 nm, which is due to the host absorption coming from the MoO_6^{6-} groups in Sr_2CaMoO_6 structure [15, 16]. However, we cannot find the possible absorption region for Eu^{3+} ion on the diffuse reflection spectra, which should be owing to the weak absorption intensities of Eu^{3+}. Further, by monitoring the $^5D_0$–$^7F_1$ magnetic dipole (MD) transition of Eu^{3+} at 594 nm, the inset of Fig. 5 gives the excitation spectra of the $Sr_2Ca_{0.8}Eu_{0.1}Na_{0.1}MoO_6$ samples obtained by sintering the precursor at different temperatures. For every sample, the spectra contain broad absorption band from 320 to 450 nm with peak maximum at 350 nm, and this is due to oxygen to molybdenum CT transition. In addition, there are two obvious characteristic Eu^{3+} excitation lines in the excitation spectra, which correspond to the transitions of $^7F_0$–$^5L_6$ at 396 nm and $^7F_0$–$^5D_2$ at 412 nm, respectively. Further, with increasing temperature, the excitation intensity increases from 1073 to 1273 K, then it decreases at 1373 K, which indicates that the sample obtained at 1273 K has the strongest excitation intensity.

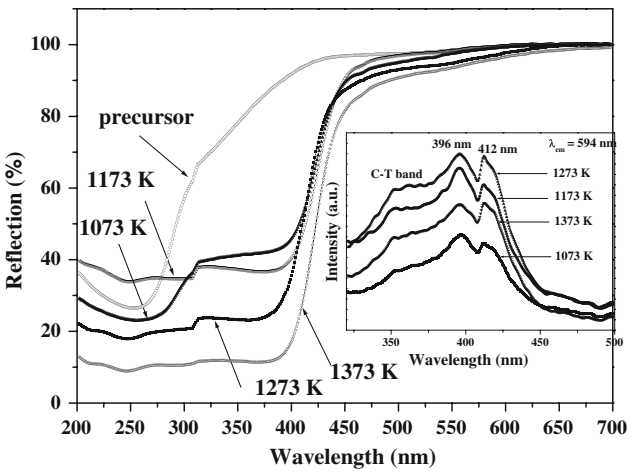

Fig. 5 Diffuse reflection spectra and excitation ($\lambda_{em} = 594$ nm) spectra (*Inset*) of the precursor and the $Sr_2Ca_{0.8}Eu_{0.1}Na_{0.1}MoO_6$ samples obtained by sintering the precursor at different temperatures

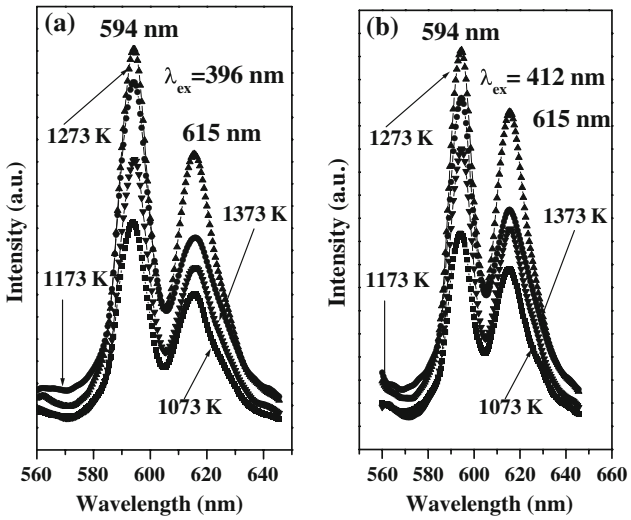

Fig. 6 Emission spectra of the $Sr_2Ca_{0.8}Eu_{0.1}Na_{0.1}MoO_6$ samples obtained by sintering the precursor at different temperatures, **a** $\lambda_{ex} = 396$ nm, **b** $\lambda_{ex} = 412$ nm

Figure 6 gives the sintering temperature-dependent emission spectra of the $Sr_2Ca_{0.8}Eu_{0.1}Na_{0.1}MoO_6$ samples. Upon different excitation wavelengths (396 and 412 nm), we can find that both emission intensities with different sintering temperatures have the same variation trend, and the sample obtained at 1273 K has the strongest emission intensity, which is consistent with the excitation spectra. For the two series samples excited by 396 or 412 nm, two typical emission peaks of Eu^{3+} are located mainly in the red region of the spectrum (594 and 615 nm) and are attributable to the $^5D_0$–$^7F_1$ and $^5D_0$–$^7F_2$ transitions, respectively. We can also find that the relative intensity of $^5D_0$–$^7F_1$ MD transition at 594 nm is higher than that of $^5D_0$–$^7F_2$ electric dipole (ED) transition at 615 nm. As mentioned earlier, Sr_2CaMoO_6 with pseudo-cubic structure has no distortional A- and B-sites in the double-perovskite structure, and the Eu^{3+} ions enter the B-sites in ABO_3 frameworks, which is the center of the cubic cell [15]. The observed characteristics Eu^{3+} luminescence in Sr_2CaMoO_6 host clearly indicates that the Eu^{3+} occupies centrosymmetric site in the currently studied phases.

It is generally accepted that effect of Eu^{3+} concentration plays an important role in the luminescence properties of the red-emitting phosphor, and the variations of luminescence properties of Eu^{3+} concentration-dependent $Sr_2Ca_{1-2x}Eu_xNa_xMoO_6$ have been investigated in this study. Figure 7 gives the diffuse reflection spectra of $Sr_2Ca_{1-2x}Eu_xNa_xMoO_6$ phosphors with different Eu^{3+}-doping concentrations, which are recorded under the same experimental conditions. All the samples show broad absorption

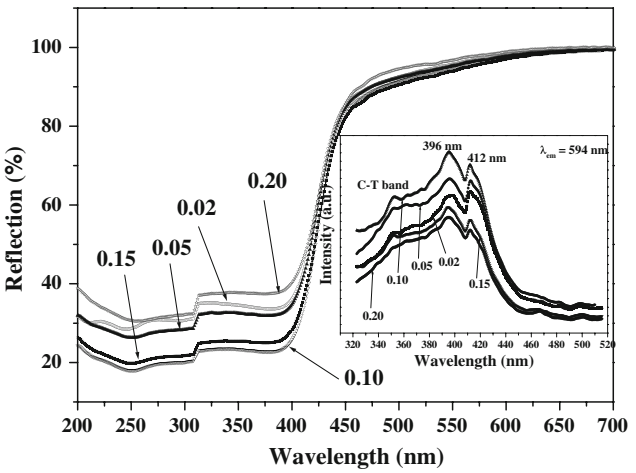

Fig. 7 Diffuse reflection spectra and excitation ($\lambda_{em} = 594$ nm) spectra (*Inset*) of $Sr_2Ca_{1-2x}Eu_xNa_xMoO_6$ ($x = 0.02$, 0.05, 0.10, 0.15, 0.2) prepared at 1273 K for 8 h

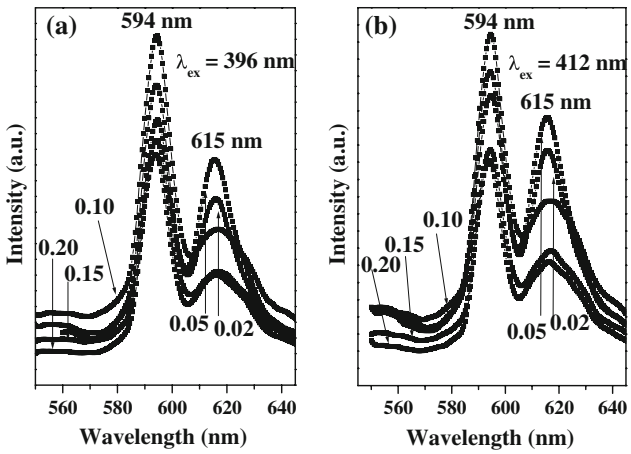

Fig. 8 Emission spectra of $Sr_2Ca_{1-2x}Eu_xNa_xMoO_6$ ($x = 0.02$, 0.05, 0.10, 0.15, 0.2) prepared at 1273 K for 8 h, **a** $\lambda_{ex} = 396$ nm, **b** $\lambda_{ex} = 412$ nm

band ranging from 200 to 450 nm, and there are three obvious absorption bands peaking at 251, 307, and 388 nm, respectively. The observed broad absorption bands are assigned to CT transition of the MoO_6^{6-} groups in Sr_2CaMoO_6 structure. Accordingly, excitation spectra obtained by monitoring the $^5D_0$–$^7F_1$ transition of Eu^{3+} at 594 nm for $Sr_2Ca_{1-2x}Eu_xNa_xMoO_6$ with varied Eu^{3+} dopant concentration are presented in the inset of Fig. 7. As stated above, the excitation spectra for various Eu^{3+} concentrations are all composed of three characteristic absorption regions, and the first one is the broad absorption band from 320 to 450 nm with peak maximum at 350 nm, which is originated from oxygen to molybdenum CT transition. Two obvious characteristic Eu^{3+} excitation lines at 396 and 412 nm are ascribed to the transitions of $^7F_0$–$^5L_6$ and $^7F_0$–$^5D_2$, respectively. Further, we can also find that $Sr_2Ca_{0.8}Eu_{0.1}Na_{0.1}MoO_6$ sample has the strongest absorption in the excitation spectra.

We should also find that the red emission is observed for all compositions with excitation either in the CT band or in the Eu^{3+} levels. The emission spectra obtained by excitation at 396 and 412 nm for $Sr_2Ca_{1-2x}Eu_xNa_xMoO_6$ ($x = 0.02$, 0.05, 0.10, 0.15, 0.2) are given in Fig. 8a and b, respectively. As seen in Fig. 8, under different Eu^{3+} excitations (396 and 412 nm), there are the same emission spectra profiles and variations. A dominant red emission line at around 594 nm, which is due to the Eu^{3+} magnetic dipole transition of $^5D_0$–$^7F_1$, is observed in the two excitation wavelengths. However, for the Eu^{3+} concentration-dependent emission spectra of $Sr_2Ca_{1-2x}Eu_xNa_xMoO_6$ phosphors, the relative intensities between $^5D_0$–$^7F_1$ and $^5D_0$–$^7F_2$ transitions have obvious difference. In order to display this variation trend obviously, Fig. 9a gives the emission intensities at 594 and 615 nm as a function of Eu^{3+}-doping concentrations for $Sr_2Ca_{1-2x}Eu_xNa_xMoO_6$ phosphors. As seen in Fig. 9a, for the emission intensities at 594 nm, it is found that the emission intensities under 396 nm have the same variation as that under 412 nm when Eu^{3+} concentrations x increases, the maximum emission intensity was observed for the Eu^{3+} concentrations $x = 0.10$. As a comparison, although the emission intensities under 396 nm are the same as that under 412 nm when Eu^{3+} concentrations x increases, the maximum emission intensity at 615 nm was observed for the second composition, viz, Eu^{3+} concentrations $x = 0.05$. Further, Fig. 9b shows the Eu^{3+}-doping concentration dependence of the relative emission intensities of $I_{594/615}$ with Eu^{3+} concentration for $Sr_2Ca_{1-2x}Eu_xNa_xMoO_6$ phosphors. We can find that the relative emission intensities of $I_{594/615}$ have the same variation. As far as the Eu^{3+}-doping concentration is concerned, there is the minimum difference between the emission intensity at 594 nm and that at 615 nm for the Eu^{3+} concentrations $x = 0.05$. With increasing Eu^{3+} concentrations, the variation of the relative emission intensities of $I_{594/615}$ keeps nearly invariable. As is well known, Eu^{3+} is a good probe for the chemical environment of the rare-earth ion because the $^5D_0$–$^7F_2$ transition is very sensitive to relatively small changes in the surroundings, but the $^5D_0$–$^7F_1$ transition is insensitive to the environment [25]. Although no obvious impurity phase can be found in $Sr_2Ca_{1-2x}Eu_xNa_xMoO_6$ solid solution even when $x = 0.20$, this is also testified by our XRD analysis. However, when excess Eu^{3+} ions enter the Ca^{2+} sites, which is ascribed to the inversion center sites, it will change the environment of Eu^{3+} in the Sr_2CaMoO_6 host lattice, and ED transition at 615 nm will decrease, then CD transition at 594 nm will be relatively strong.

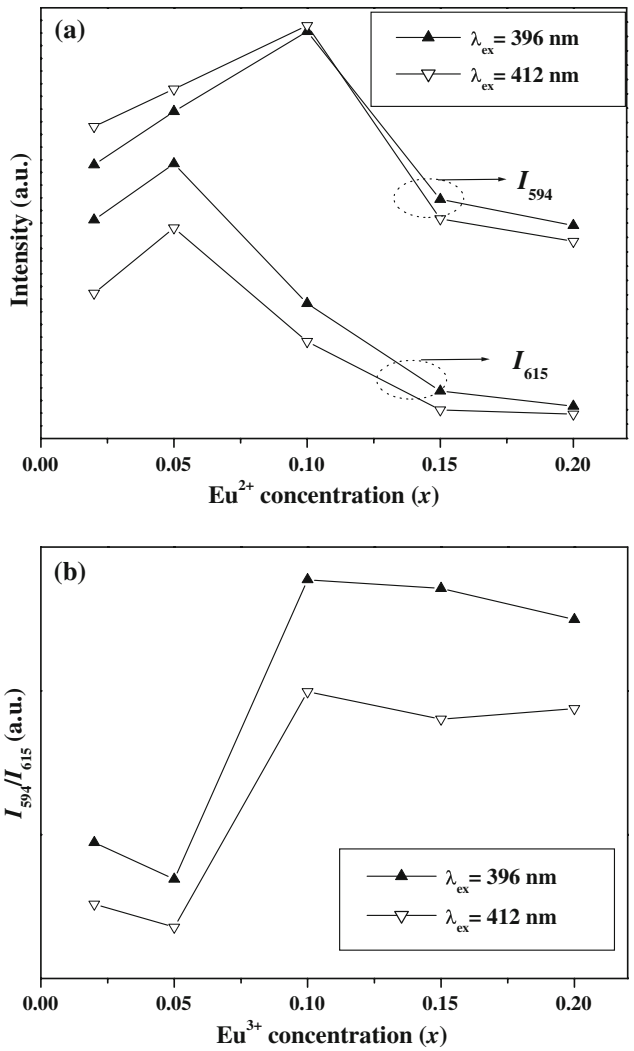

Fig. 9 Variation of emission intensities at 594 and 615 nm (**a**) and the relative emission intensities of $I_{594/615}$ (**b**) with Eu^{3+} concentration for $Sr_2Ca_{1-2x}Eu_xNa_xMoO_6$ ($x = 0.02$, 0.05, 0.10, 0.15, 0.2) prepared at 1273 K for 8 h

Conclusions

A series of double-perovskite $Sr_2Ca_{1-2x}Eu_xNa_xMoO_6$ red-emitting phosphors was prepared by the citric acid-assisted sol–gel method. $Sr_2Ca_{0.8}Eu_{0.1}Na_{0.1}MoO_6$ phosphor was selected to study the thermal behavior, phase structure, microstructure, and photoluminescence property under different sintering temperatures. The optimum synthesis temperature by sol–gel process can be decided as 1273 K. And at this temperature, $Sr_2Ca_{0.8}Eu_{0.1}Na_{0.1}MoO_6$ phosphor with pure phase, uniform microstructure, and optimum luminescence properties can be found. The photoluminescence studies on $Sr_2Ca_{1-2x}Eu_xNa_xMoO_6$ ($x = 0.02$, 0.05, 0.10, 0.15, 0.2) show that a dominant red emission line at around 594 nm is observed under different Eu^{3+} excitations (396 and 412 nm). Eu^{3+}-doping concentration-dependent emission spectra investigations of $Sr_2Ca_{1-2x}Eu_xNa_xMoO_6$ phosphors indicate that there are the minimum differences between the emission intensity of $^5D_0$–$^7F_1$ transition at 594 nm and that of $^5D_0$–$^7F_2$ transition at 615 nm when the Eu^{3+} concentrations $x = 0.05$. Since Eu^{3+} ions enter the inversion center Ca^{2+} sites, the intensity of $^5D_0$–$^7F_1$ transition at 615 nm will decrease, then the emission of $^5D_0$–$^7F_2$ transition at 594 nm will be relatively strong. Therefore, the variation of the above two emission intensities keeps nearly invariable with increasing Eu^{3+} concentration.

Acknowledgements This study was supported by the Ph.D. Programs Foundation of Ministry of Education of China (Grant No. 20090022120002), the National Natural Science Foundations of China (Grant No. 20876002 and No. 20976002), the Beijing Natural Science Foundation (Grant No. 2082009 and No. 2091002), and the College Student Research Innovation Program of China University of Geosciences, Beijing.

References

1. Nakamura S, Fasol G (1997) The blue laser diode: GaN based light emitters and lasers. Springer, Berlin, p 19
2. Nakamura S, Snoh M, Mukai T (1993) Appl Phys Lett 62:2390
3. Chan T, Liu R, Baginskiy I (2008) Chem Mater 20:1215
4. Park JK, Kim CH, Park SH, Park HD (2004) Appl Phys Lett 84:1647
5. Neeraj S, Kijima N, Cheetham AK (2004) Chem Phys Lett 387:2
6. Liu J, Lian H, Shi C (2007) Opt Mater 29:1591
7. Uheda K, Hirosaki N, Yamamoto Y, Natio A, Nakajima T, Yamamoto H (2006) Electrochem Solid-State Lett 9:H22
8. Sivakumar V, Varadaraju UV (2005) J Electrochem Soc 152: H168
9. Wang J, Jing X, Yan C, Lin J, Liao F (2005) J Electrochem Soc 152:G534
10. Zhang Q, Wang J, Yu R, Zhang M, Su Q (2008) Electrochem Solid-state Lett 11:H335
11. Wang J, Jing X, Yan C, Lin J, Liao F (2006) J Lumin 121:57
12. Guo C, Chen T, Luan L, Zhang W, Huang D (2008) J Phys Chem Solids 69:1905
13. Shi S, Gao J, Zhou J (2008) J Electrochem Soc 155:H525
14. Chiu C, Liu C, Huang S, Chen T (2008) J Electrochem Soc 155:J71
15. Ye S, Wang C, Jing X (2008) J Electrochem Soc 155:J148
16. Ye S, Wang C, Liu Z, Lu J, Jing X (2008) Appl Phys B 91:551
17. Sivakumar V, Varadaraju UV (2008) J Solid State Chem 181: 3344
18. Guo C, Zhang W, Luan L, Chen T, Cheng H, Huang D (2008) Sensor Actuat B-Chem 133:33
19. Prior T, Couper V, Battle P (2005) J Solid State Chem 178:153
20. Teraoka Y, Wei MD, Kagawa S (1998) J Mater Chem 8:2323
21. Tomaszewicz E (2006) Solid State Sci 8:508
22. Lei F, Yan B (2008) J Solid State Chem 181:855
23. Anderson MT, Greenwood KB, Taylor GA, Poeppelmeier KR (1993) Prog Solid State Chem 22:197
24. Lei F, Yan B, Chen H (2008) J Solid State Chem 181:2845
25. Pang ML, Liu XM (2005) J Mater Res 20:2676